Fracture network analysis in the Duke River area, southwestern Yukon

F.M. Chapman*, M. Miranda, R. Soucy La Roche and J. Raymond
Institut national de la recherche scientifique (Centre Eau Terre Environnement, Québec, QC)

Abstract

Deep geothermal reservoir potential depends on the local temperature gradient and host rock permeability. In areas with low primary porosity, such as the Duke River area, large-scale permeability is primarily associated with fracture networks. Fractures in the Duke River area are described based on 36 scanlines collected across 9 rock types from 0.8 to 22 km from the Denali fault. The majority of fractures are steeply dipping but have no preferential strike. The linear fracture intensity is high, and most fractures range from open to moderately wide. These attributes vary slightly by lithology but can be grouped into distinct hydrostratigraphic units. The distance from the Denali fault has a non-linear influence on fracture intensity and aperture and a negligible effect on fracture spacing and length. The fracture analysis presented will be used to develop a discrete fracture network to evaluate permeability in the Duke River area.

* fiona.chapman@inrs.ca

Introduction

This research is part of an on-going project to evaluate the deep geothermal potential in the Duke River area, southwestern Yukon. The Duke River area was selected as a study site due to a promising temperature gradient measured in a shallow well, elevated Curie point depth and potential for elevated permeability due to extensive fracturing of the bedrock associated with the Denali fault (e.g., Witter, 2020). Extensional fractures can be important conduits for geothermal fluids in hard rock areas where the primary porosity is low, such as in the Duke River area (Singhal and Gupta, 2010).

Fractures is an all-encompassing term to denote a planar surface, with at some scale, an opening (Fossen, 2010). Fractures occur as a result of external (e.g., tectonic) or internal (e.g., thermal) stress (Fossen, 2010). They include shear fractures (or faults) and extensional fractures (joints, fissures, veins and dikes; Fossen, 2010). The strike of fractures and their apertures will depend on the principal stresses. Here, we are interested in the impact of fractures on subsurface permeability. Fracture-derived permeability depends on geometric fracture attributes, such as fracture density, spacing, length, aperture and connectivity (Singhal and Gupta, 2010). Therefore, it is essential to describe regional fracture networks prior to estimating permeability and defining reservoir potential. The permeability is an important hydrogeological characteristic which contributes to potential reservoir productivity, be it for drinking water or open-loop geothermal systems (Singhal and Gupta, 2010).

In southwestern Yukon, the shallow (385 m) temperature gradient in Quaternary sediments that overlay the Denali fault is characteristic of conductive heat transfer (F. Chapman, unpublished data). However, elevated topography such as around the Denali fault provides an ideal geological context for forced convection to occur (e.g., Morgan et al., 1981; Štulc, 1998; Saar, 2010; Townend et al., 2017). The differences in surface pressures and hydraulic head on either side of the Denali fault is expected to force meteoric water into deep circulation where it can be heated before rising toward Kluane Lake at lower elevation. The spatial distribution of permeability in the Duke River area influences regional groundwater flow and convection potential.

Fractures in the Duke River area are thought to be associated, at least in part, with stresses that caused the Denali fault. The objective of this research is to evaluate the influence of lithology and fault proximity on regional scale fracture networks around the Denali fault to better understand the spatial distribution of permeability. We are interested in large scale permeability to understand the potential for convective heat transfer that can affect the extent of geothermal resources. We therefore evaluated fracture networks on a regional scale (e.g., Camanni et al., 2021): up to 24 km from the Denali fault and across nine different rock types. We hypothesize that geometric fracture attributes (linear fracture intensity, fracture length and fracture aperture) will decrease with distance from the fault. The results of this regional scale analysis will inform future research wherein the spatial distribution of permeability will be integrated into a coupled heat-flow model to quantify geothermal potential based on conductive and advective heat transfer.

Geological setting

Canadian Cordillera

The Canadian Cordillera is an orogenic belt composed of a collage of allochthonous terranes (Colpron et al., 2007) that were accreted to autochthonous and parautochthonous units of the western margin of Laurentia. The terranes that make up the Canadian Cordillera are primarily sedimentary basins and platforms, magmatic arcs, and microcontinents, which can be grouped into four categories: Intermontane terranes, Insular and Northern Alaska terranes, Oceanic and accretionary complex terranes, and Mesozoic and younger arc and accretionary terranes (Fig. 1; Colpron et al., 2007; Nelson and Colpron, 2007). Accretion of the Canadian Cordillera was ongoing during the Late Triassic to earliest Jurassic (Colpron et al., 2015, 2022; George et al., 2021), and possibly started as early as late Permian (Beranek and Mortensen, 2011) and continues today with the Yakutat microplate collision along the southern Alaskan coast (Elliott et al., 2010).
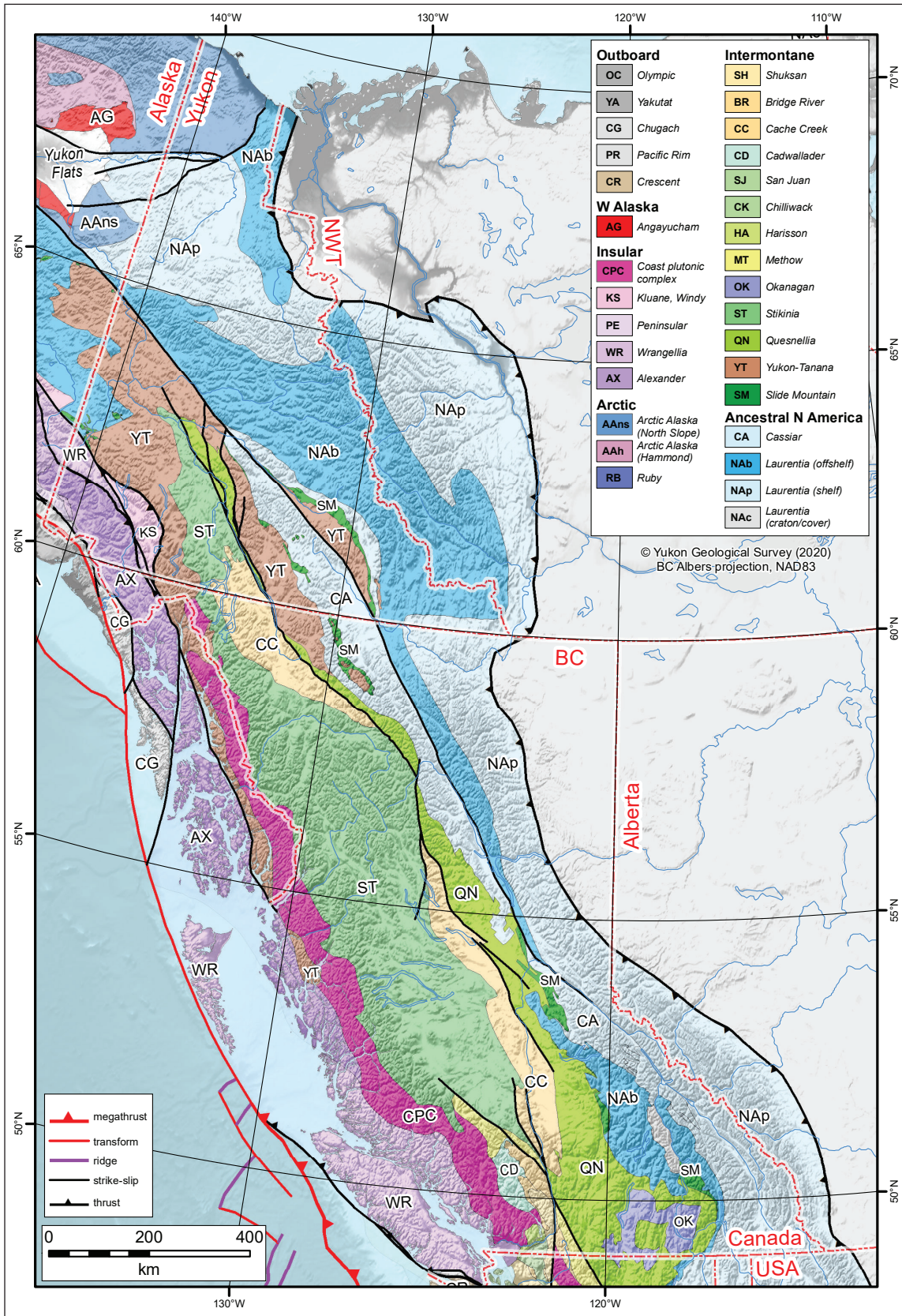
Figure 1. Distribution of terranes of the Canadian Cordillera (Yukon Geological Survey, 2020).

Denali fault

The Denali fault is a major right-lateral strike-slip fault in the Canadian Cordillera which extends over 2000 km across central Alaska, through southwestern Yukon, and into northern British Columbia (Fig. 1; Nelson and Colpron, 2007; Choi et *al.*, 2021). In southwestern Yukon, the eastern Denali fault separates the Alexander and Wrangellia terranes on the southwest from metamorphic rocks of the Kluane schist and the Yukon-Tanana terrane on the northeast (Fig. 1). Since the Early Cretaceous, the Denali fault has accommodated a dextral displacement of ~400–480 km (Lowey, 1998; Waldien et *al.*, 2021). Today, the eastern Denali fault experiences less activity than the Alaska portion of the Denali fault (Bender and Haeussler, 2017; Blais-Stevens et *al.*, 2020). This is reflected in the present-day average slip rate of ~5 to 12 mm per year along the east-west striking Alaskan portion of the Denali fault, compared to ~2 to 5 mm per year along the southeast–northwest striking eastern Denali fault which passes through Yukon and British Columbia (Leonard et *al.*, 2008; Haeussler et *al.*, 2017; Blais-Stevens et *al.*, 2020). Though strike-slip displacement along the eastern Denali fault is dominant, vertical displacement of 0.2 to 0.9 mm per year has been reported (Marechal et *al.*, 2018; McDermott et *al.*, 2019).

Study site

Increased permeability due to brittle fracturing is expected along the Denali fault relative to other areas in Yukon due to the recent activity, including seismic shaking in the past 6000 years (Blais-Stevens et *al.*, 2020). A transtensional pull-apart was identified along the Denali fault near the community of Burwash Landing in southwestern Yukon where the main fault is mapped as three fault strands, though only a single strand has had a visible effect on the overlying sediments (Witter, 2020; Finley et *al.*, 2022; Tschirhart et *al.*, 2022). This releasing bend is expected to generate an area of increased local permeability. Faulds and Hinz (2015) associated transtensional pull-aparts along strike-slip faults with increased local permeability, such as in the Great Basin Region, USA, where this tectonic setting houses 3% of mapped geothermal fields.

The Duke River area, southwest of the Denali fault between Duke River and Congdon Creek, was previously mapped by Israel et *al.* (2006; Fig. 2). The area is underlain by rocks of Wrangellia and the Alexander terrane to the south. The Ruby Range batholith and Kluane schist occur northeast of the Denali fault. Late Paleozoic to mid-Cretaceous plutons are distributed throughout the Wrangellia and Alexander terranes (Colpron et *al.*, 2016).

The study area is bound to the southwest by flow divides and to the northeast by the Kluane Lake (Fig. 2), which form no flow or constant hydraulic head boundaries that will facilitate the integration of fracture analysis results into a hydrothermal model to quantify geothermal resources. Figure 3 is a conceptual model which will be the basis for a quantitative groundwater flow model in future research. Fracture measurements were taken along several transects to ensure that fracture measurements for all pertinent rock types were collected on representative outcrops.

Lithological units

All the lithological units defined by Israel et *al.* (2006) in Wrangellia (WR), overlap assemblages (OA), intrusive rocks (IR) and Alexander terrane (AX), as well as the Kluane schist crop out in the study area (Figs. 2 and 4). Descriptions of lithological units are based on Israel et *al.* (2006) and were complemented by our field observations. The dominant units exposed on the south side of the fault are the Station Creek and Hasen Creek formations of the Skolai Group, and the Nikolai formation (all units of WR). The Station Creek Formation is a Pennsylvanian to Permian volcanic unit including breccia, crystallithic tuffs, tuffaceous siltstone, and augite-phyric basalt flows. The thickness is poorly constrained but is at least several hundred metres. The lower Permian Hasen Creek Formation overlies the Station Creek Formation and is dominated by fossiliferous siltstone, turbidites and mudstones in the Duke River area. The Upper Triassic Nikolai formation consists of basalt flows around 1000 m thick in the Kluane Ranges.
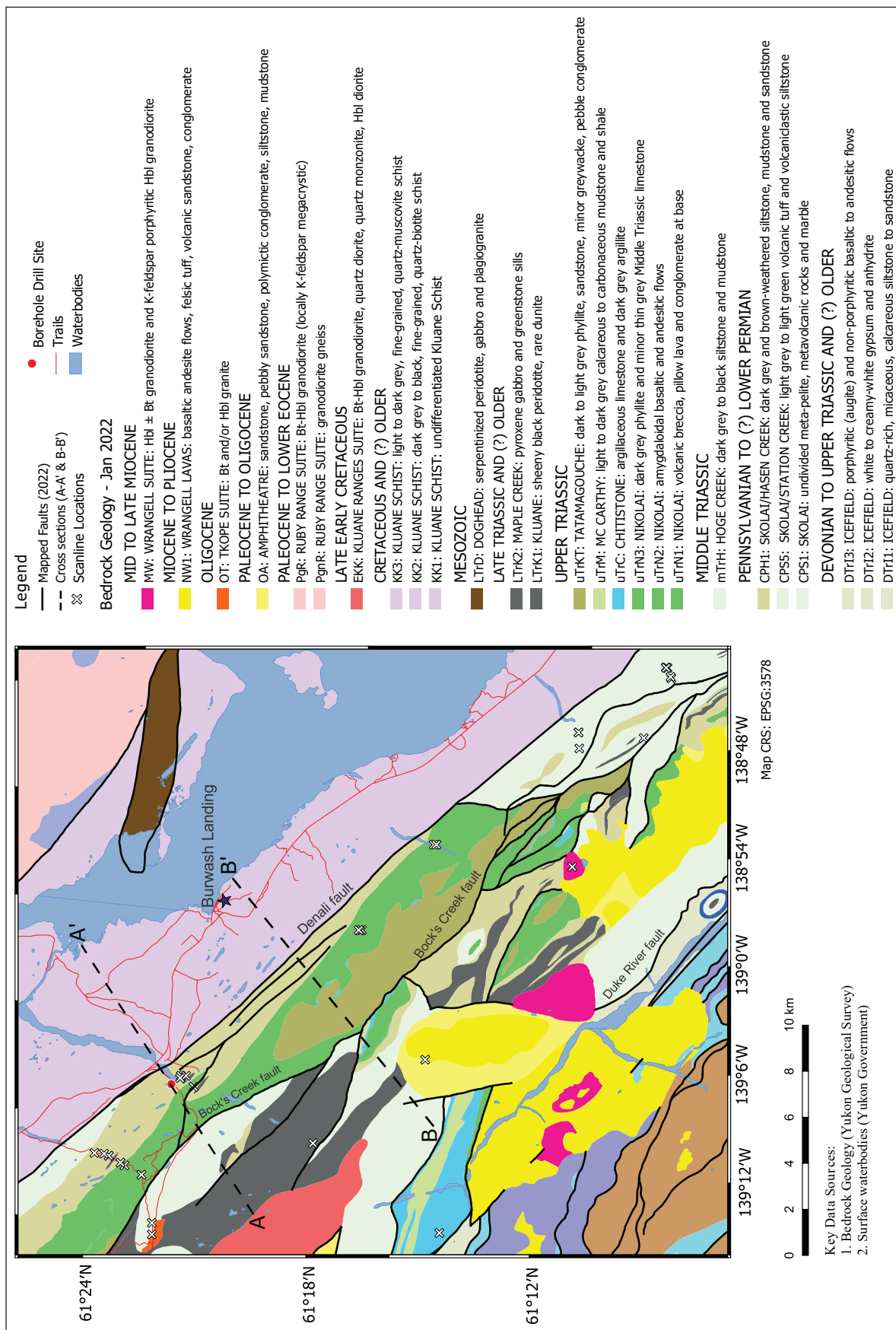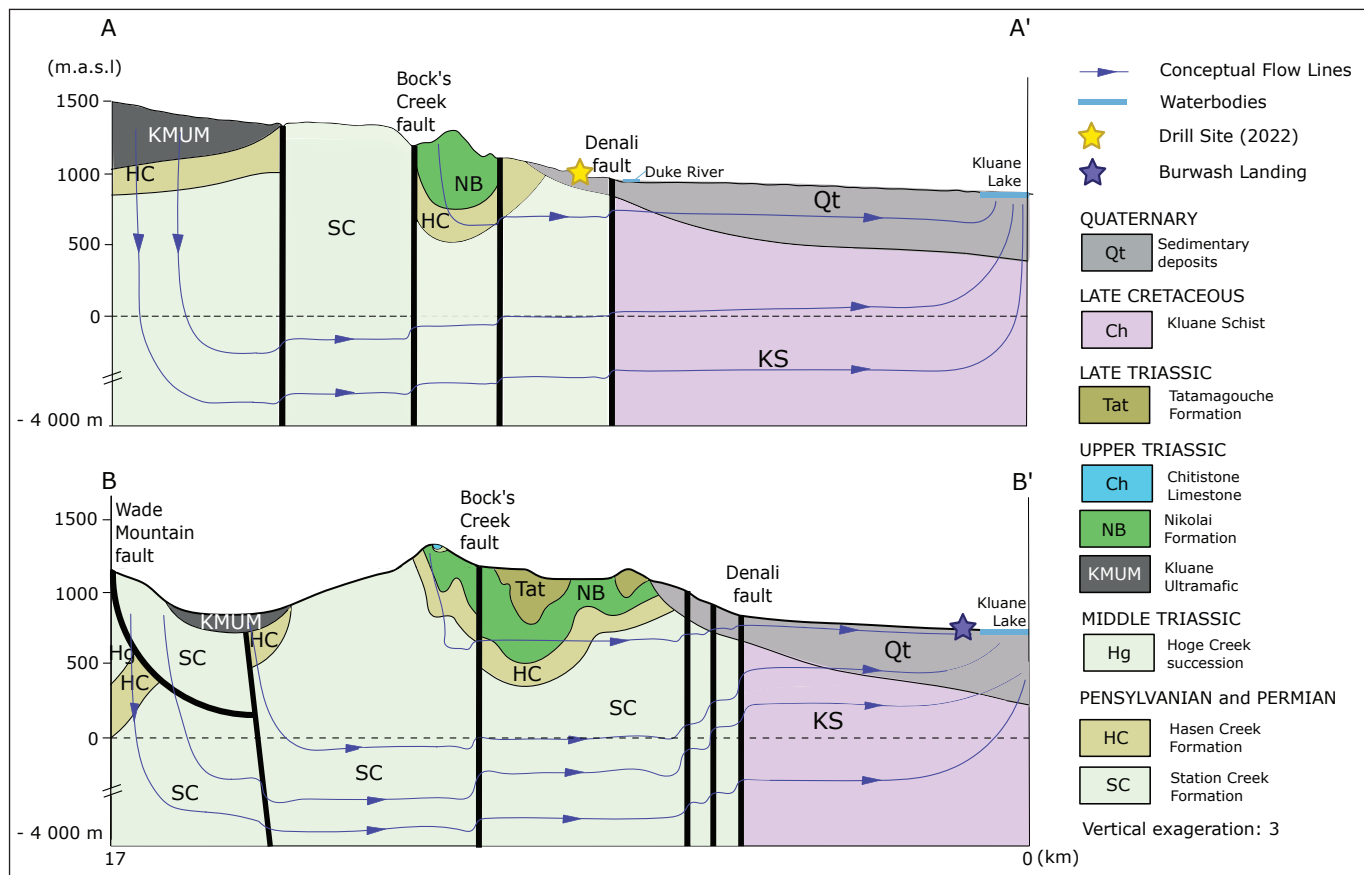
Legend

Mapped Faults (2022)

Cross sections (A–A' & B–B')

Scanline Locations

● Borehole Drill Site

Trails

Waterbodies

Bedrock Geology - Jan 2022

MID TO LATE MIOCENE
MW: WRANGELL SUITE: Hbl ± Bt granodiorite and K-feldspar porphyritic Hbl granodiorite

MIOCENE TO PLIOCENE
NW1: WRANGELL LAVAS: basaltic andesite flows, felsic tuff, volcanic sandstone, conglomerate

OLIGOCENE
OT: TKOPE SUITE: Bt and/or Hbl granite

PALEOCENE TO OLIGOCENE
OA: AMPHITHEATRE: sandstone, pebbly sandstone, polymictic conglomerate, siltstone, mudstone

PALEOCENE TO LOWER EOCENE
PgR: RUBY RANGE SUITE: Bt-Hbl granodiorite (locally K-feldspar megacrystic)
PgnR: RUBY RANGE SUITE: granodiorite gneiss

LATE EARLY CRETACEOUS
EKK: KLUANE RANGES SUITE: Bt-Hbl granodiorite, quartz diorite, quartz monzonite, Hbl diorite

CRETACEOUS AND (?) OLDER
KK3: KLUANE SCHIST: light to dark grey, fine-grained, quartz-muscovite schist
KK2: KLUANE SCHIST: dark grey to black, fine-grained, quartz-biotite schist
KK1: KLUANE SCHIST: undifferentiated Kluane Schist

MESOZOIC
LTrD: DOGHEAD: serpentinized peridotite, gabbro and plagiogranite

LATE TRIASSIC AND (?) OLDER
LTrK2: MAPLE CREEK: pyroxene gabbro and greenstone sills
LTrK1: KLUANE: sheeny black peridotite, rare dunite

UPPER TRIASSIC
uTrKT: TATAMAGOUCHE: dark to light grey phyllite, sandstone, minor greywacke, pebble conglomerate
uTrM: MC CARTHY: light to dark grey calcareous to carbonaceous mudstone and shale
uTrC: CHITISTONE: argillaceous limestone and dark grey argillite
uTrN3: NIKOLAI: dark grey phyllite and minor thin grey Middle Triassic limestone
uTrN2: NIKOLAI: amygdaloidal basaltic and andesitic flows
uTrN1: NIKOLAI: volcanic breccia, pillow lava and conglomerate at base

MIDDLE TRIASSIC
mTrH: HOGE CREEK: dark grey to black siltstone and mudstone

PENNSYLVANIAN TO (?) LOWER PERMIAN
CPH1: SKOLAI/HASEN CREEK: dark grey and brown-weathered siltstone, mudstone and sandstone
CPS5: SKOLAI/STATION CREEK: light grey to light green volcanic tuff and volcaniclastic siltstone
CPS1: SKOLAi: undivided meta-pelite, metavolcanic rocks and marble

DEVONIAN TO UPPER TRIASSIC AND (?) OLDER
DTrI3: ICEFIELD: porphyritic (augite) and non-porphyritic basaltic to andestic flows
DTrI2: ICEFIELD: white to creamy-white gypsum and anhydrite
DTrI1: ICEFIELD: quartz-rich, micaceous, calcareous siltstone to sandstone

Key Data Sources:
1. Bedrock Geology (Yukon Geological Survey)
2. Surface waterbodies (Yukon Government)

Map CRS: EPSG:3578

Figure 2. Geological map of the Duke River and surrounding area *(Yukon Geological Survey, 2022).*

Figure 3. *Conceptual groundwater flow model for two cross sections of interest in the Duke River area. The location of cross section A-A' and B-B' are indicated in Figure 2. The geological cross sections are based on geological bedrock mapping, field observations, and cross sections presented in Israel et al. (2006). The geological units were extended below sea level with uncertainty as the thickness of the Station Creek Formation and Kluane schist are unknown. Flow lines present potential flow pathways. The mapped fault dips are also poorly to not defined in the area and are extended with uncertainty.*

Less volumetrically important units that are also exposed on the southwest side of the Denali fault include:

1. the Middle Triassic Hoge Creek succession (WR), a thin and discontinuous sedimentary layer;

2. the Upper Triassic Chitistone Limestone (WR) of variable thickness (hundreds of metres to discontinuous lenses);

3. the Upper Triassic McCarthy Formation (WR), a highly folded sedimentary layer primarily found in Hoge Creek syncline;

4. the Upper Triassic to Lower Cretaceous Tatamagouche succession composed of marine clastic sedimentary rocks (OA); and

5. the Eocene to Oligocene terrestrial sedimentary rocks of the Amphitheatre Formation and Wrangell Lavas (OA).

Intrusive rocks include the Late Triassic Maple Creek gabbro and Kluane mafic-ultramafic complex, the Early Cretaceous Kluane Ranges suite, the Oligocene Tkope suite, and the Miocene Wrangell suite. The Kluane mafic-ultramafic complex is the most extensive intrusive unit in the Duke River area. The thickness of the Kluane mafic-ultramafic complex is poorly defined but it is inferred to underlie the Burwash Uplands.
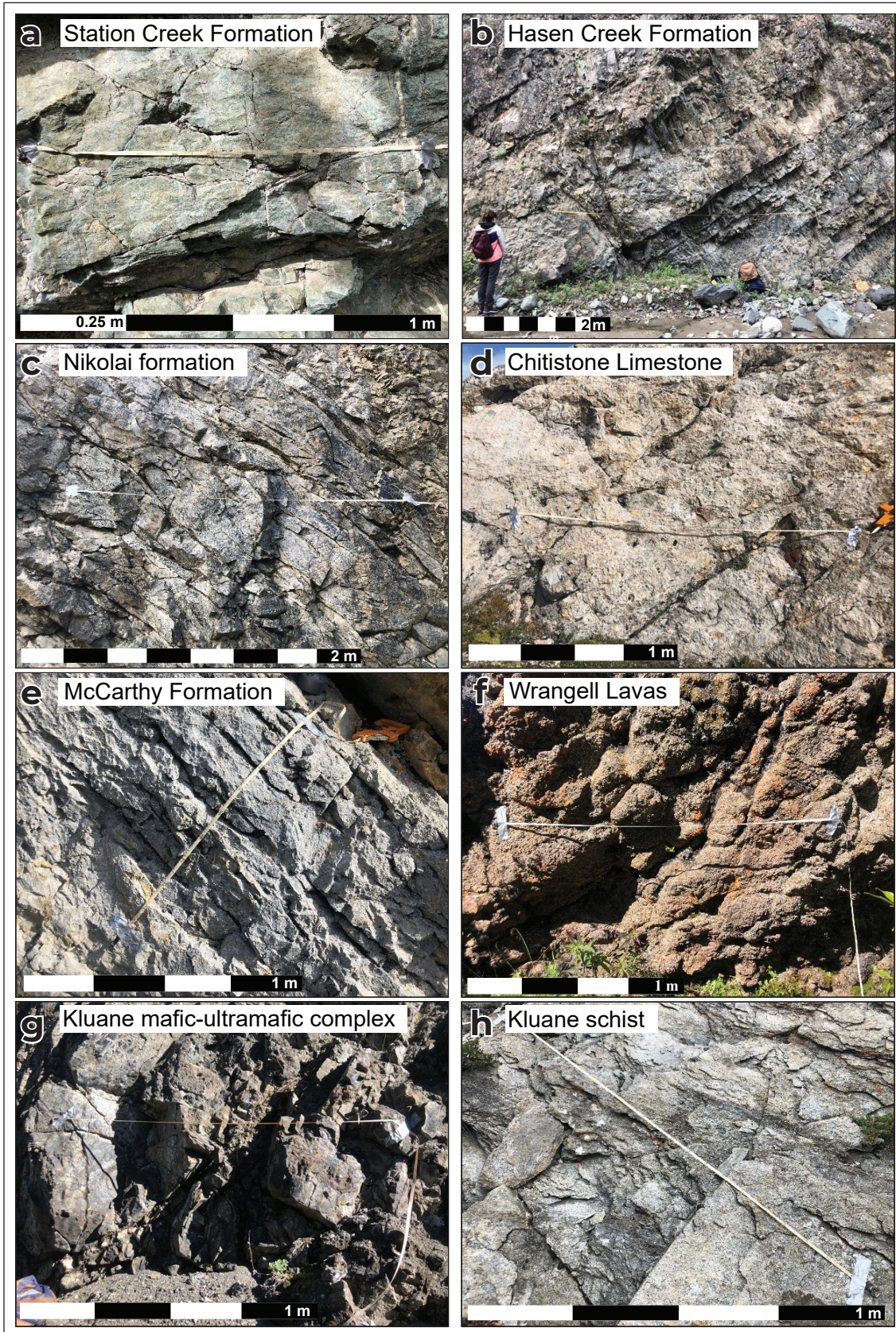
Figure 4. *Outcrop examples of each accessible unit in the study area.*

The Late Cretaceous Kluane schist is a highly deformed metasedimentary unit on the northeastern side of the Denali fault (Mezger et a*l*., 2001a; Stanley, 2012). The Kluane schist exposed northeast of Kluane Lake extends beneath at least 380 m of Quaternary sediments near the Denali fault southwest of the lake. The metamorphic grade of the Kluane schist decreases southwestward from amphibolite facies near the Paleocene Ruby Range batholith to greenschist facies closest to the Denali fault (Mezger et a*l*., 2001b; Stanley, 2012).

Methods

Sampling locations

The study area is mountainous, with creeks that carve through the mountains. These creeks are inlets to Kluane Lake. Throughout the field campaign, most outcrops used for fracture measurements were reached on foot along the creeks. A total of 35 outcrops were accessed southwest of the Denali fault, either along creeks: Congdon Creek, Nines Creek, Bock's Creek, Lewis Creek, Copper Joe Creek, Duke River, Burwash Creek, or by helicopter on August 13, 2022. General areas were identified prior to the field campaign using the Yukon Geological Survey bedrock geology map (2022) to ensure that measurements were taken to be representative of each lithology. Potential outcrops were identified remotely prior to fieldwork but the outcrop exposure and accessibility were uncertain due to the quality of available satellite images. The final outcrops were identified on site.

There are no Kluane schist outcrops in the study area. One Kluane schist outcrop was accessed on the northeast side of Kluane Lake and the study area. Future sites have been identified based on Stanley (2012) to describe the Kluane schist but require a helicopter assist. These sites are expected to be representative of the Kluane schist below the Quaternary sediments southwest of Kluane Lake northeast of the Denali fault.

Field data acquisition

Fracture data were collected by manual fracture measurements. Manual observations were selected over digital methods, such as lidar or other GIS methods, due to interest in the variation of fracture networks between units and at varying distances from the Denali fault. Manual observations allow for recording micro and macro-fractures on outcrops which is required to study the influence of lithology on fracture attributes (Formenti et a*l*., 2022).

Fracture measurements

In this study, we use the linear scanline method. The linear scanline method is commonly used to evaluate fractures on outcrops, in borehole imagery, and on core samples (Zeeb et a*l*., 2013). The linear scanline method involves measuring fracture attributes (strike, dip, spacing, length and mechanical aperture) of all the fractures which cross the scanline (Watkins et a*l*., 2015). Measurements were taken by the same observer for each scanline to minimize observational bias (Andrews et a*l*., 2019; Formenti et a*l*., 2022). A tagline was set up along the outcrop to delineate the scanline with a length that was determined based on the size of the outcrop and the fracture density. When not limited by the size of the outcrop, at least 20 fracture measurements were taken per scanline, which ranged from 0.47 m to 2.86 m.

The fracture strike and dip were measured using the FieldMove Clino App by Midland Valley. FieldMove Clino is a digital compass-clinometer designed for smartphones (Vaughn et a*l*., 2014). This accelerates the rate at which planar and linear field measurements can be taken and georeferenced directly onto a basemap (Vaughn et a*l*., 2014).

Fracture spacing was determined based on the position of the fracture along the tagline. The length of fractures was measured below the scanline unless the fracture only projected above the scanline. These fracture measurements provide a relative length, but not absolute length of exposed fracture. The majority of fractures continue above the scanline and may extend beyond the visible outcrop. This results in truncation bias (Zeeb et a*l*., 2013). Fracture aperture was recorded using a digital caliper. For fractures with consistent aperture, the aperture was measured at the scanline. For fractures with variable aperture, an aperture measurement was taken above and below the scanline and a range was assigned. Closed fractures were assigned an aperture of zero. The aperture of

filled fractures was measured but fractures were noted as being filled or partially filled. Where possible, the mineral filling the fractures was described. The fracture data are presented based on the percent of fractures filled per scanline.

Scanline data collected

Overall, fracture data were collected on the following units (number of scanlines, s; number of fracture measurements, f): Station Creek Formation (s = 10; f = 270); Hasen Creek Formation (s = 8; 138), Nikolai formation (s = 9; f = 203); Kluane mafic-ultramafic complex (s = 2; f = 62); McCarthy Formation (s = 3; f = 31); Chitistone Limestone (s = 1; f = 9); Wrangell Lavas (s = 1; f = 17); Wrangell plutonic suite (s = 1; f = 31); Kluane schist (s = 1; f = 4).

Fracture data analysis

Fracture orientation

Stereonet version 11.4.5 (Allmendinger, 2022) is used to visualize orientation of fracture data. Rose diagrams of strike are used to visualize the distribution of fracture strike for each fracture category (all fractures, open fractures, filled and partially filled fractures, and closed fractures).

A Mixture of von Mises (MvM) distribution was used to identify fracture families based on strike following the approach outlined in Chabani et *al*. (2020). Fracture families are represented in the distribution as components (H). The optimal number of components for each fracture category are unknown. Therefore, multiple models are fit to each fracture family to determine the most representative number of components based on a combination of the negative log-likelihood of each distribution and geological feasibility. Statistically, minimizing the negative log-likelihood provides the best fit of the distribution. However, understanding the fracture data is essential to determine the true number of fracture families (or components; H) in the data. The MvM distributions for varying components were determined using the fit_vmmix function from the R package "BAMBI" which encompasses the log-likelihood (logLik; Chakraborty and Wong, 2021).

A description of the MvM distribution is provided in Appendix A.

Fracture data are projected to poles and contoured in Stereonet version 11.4.5. (Allmendinger, 2022). Kamb contours with a contour interval of a standard deviation is used with a significance level of $3 \times$ standard deviation used to contour the poles (Allmendinger, 2022). Kamb contours are based on the binomial probability distribution of the data and are used to describe the dominant dip of each facture category (Haneberg, 2004).

Geometrical fracture attributes

The fracture data were analyzed first with respect to the geometrical fracture attributes: length, aperture, spacing and intensity. Prior to the analysis, the required corrections were applied to the scanline data. There are no corrections required for the fracture length or aperture measured in the field. However, not all fracture data were collected on fractures perpendicular to the scanline. Therefore, the Terzaghi correction must be applied to correct the spacing between fractures (Equation 1; Tang et a*l*., 2016).

$$S = S_{apparent} \times |cos\,(a - a')| \qquad (1)$$

where S is the corrected spacing, $S_{apparent}$ is the recorded spacing, a (°) is the strike of the fracture and a' (°) is the strike of the scanline.

The scanline length is adjusted such that the start and end of the scanline are delimited by the first and last fracture (Sanderson and Peacock, 2019). The position of each fracture along the scanline must be adjusted by:

$$P = P - P_i \qquad (2)$$

where P (m) is the position of the fracture measurement within a scanline, and P_i (m) is the initial position of the first fracture along the scanline. The length of the scanline can then be calculated by:

$$L = P_f - P_i \qquad (3)$$

where L is the scanline length (m), P_f (m) is the position of the last measured fracture along a scanline and P_i (m) is the position of the first fracture in the scanline.

The linear fracture intensity (I; m^{-1}) can then be calculated by:

$$I = \frac{N}{L} \tag{4}$$

where N is the number of fractures which cross the scanline and L is the scanline length.

The coefficient of variation (CV) of fracture spacing describes fracture distribution and is calculated by:

$$CV = \frac{\sigma_s}{\mu_s} \tag{5}$$

where σ_s is the standard deviation and μ_s is the mean fracture spacing (Glaas et a*l*., 2021).

Lithology and Distance from the Denali fault

Geometric fracture parameters are evaluated for each set of fracture measurements based on lithology and distance from the Denali fault. The distance from the Denali fault to the scanline is measured in QGIS perpendicular to the surface map trace (Bender and Haeussler, 2017). An ANCOVA test is used to evaluate the influence of lithology on geometric fracture attributes independent of distance from the fault. The ANCOVA test is limited to data within the first 4 km from the fault where data are abundant. A pairwise t-test is used to compare rock types across the whole study area.

## Results

Fracture orientation

The best-fit number of fracture families was determined based on a combination of the lowest log-likelihood and geological feasibility. The number of fracture families is equivalent to the number of components (H) in the MvM distribution for each fracture category. The constraints imposed by Chabani et a*l*. (2020) were used to evaluate the geological feasibility of the statistically optimal

number of fracture families. Fracture families with dispersion parameter (k) less than 8 are considered not geologically feasible, as the range of values that would fall within the group is not representative of a fracture family. Fracture families with dispersion parameter greater than 32 were also discarded as these are uninformative (equivalent to a standard deviation of less than 10°). Finally, models with weightings of less than 10% were also discarded. As a result, the number of components chosen were not consistently those with the lowest log-likelihood (Fig. 5).

Based on the best-fit number of fracture families and geological feasibility of suggested fracture families, there is no preferential strike considering all fracture data (H = 4) or for open fractures (H = 4). For both categories, the four fracture families are near-equally distributed and the difference in weight between fracture families is not significant. The filled fractures can be represented by six fracture families (H = 6). The difference in weight between fracture families is also not significant; however the mean strike of fracture families ranges from NE–SW to SE–NW, with no N–S oriented fracture families. The closed fractures are also represented by six fracture families (H = 6), which range in strike from WSW–ENE to NW–SE. The dominant fracture family (F2) is oriented around a mean strike of 86.5° (E–W).

Fracture dip

There is a tendency towards steeply dipping fractures for open and filled fractures with median dips of 64.6° and 62.2°, respectively. All fracture data and the open fracture data show a left-skewed distribution (Fig. 6). The median dip of filled fractures is 62.8°. The median dip of closed fractures is 51.8° but have a bimodal distribution with the greatest number of dips ranging between 35° and 45°, and 75° and 85°.
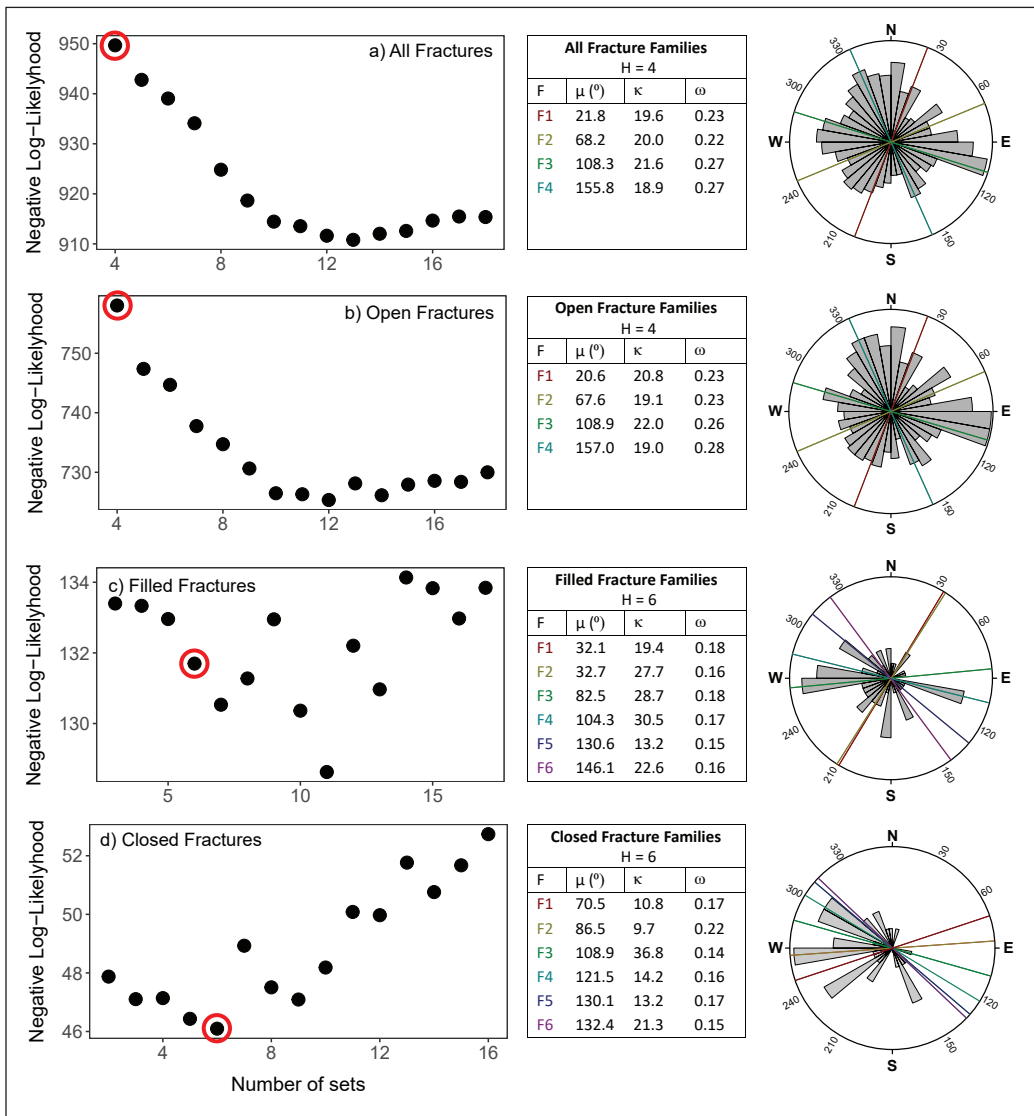
Figure 5. *The fracture families determined based on the negative log-likelihood and geological feasibility of statistically defined fracture families. The number of fracture families identified based on these conditions is circled in red to highlight the respective log-likelihood.*

Average geometric fracture attributes

The geometric fracture attributes measured are the fracture linear intensity, spacing, length and aperture. These are summarized for each fracture family (Table 1). The median linear fracture intensity is 13.7 fractures per metre whereas the mean spacing of all fractures is 0.04 m. However, the spacing is highly variable. The mean length of open fractures is longer than both the filled and closed fractures. The fracture apertures are highly variable, but the majority are considered open to moderately wide on the ISRM (1978) fracture aperture scale (Table 2). The fracture apertures show a scale dependence based on fracture length (Fig. 7a) but no correlation with fracture strike (Fig. 7b).
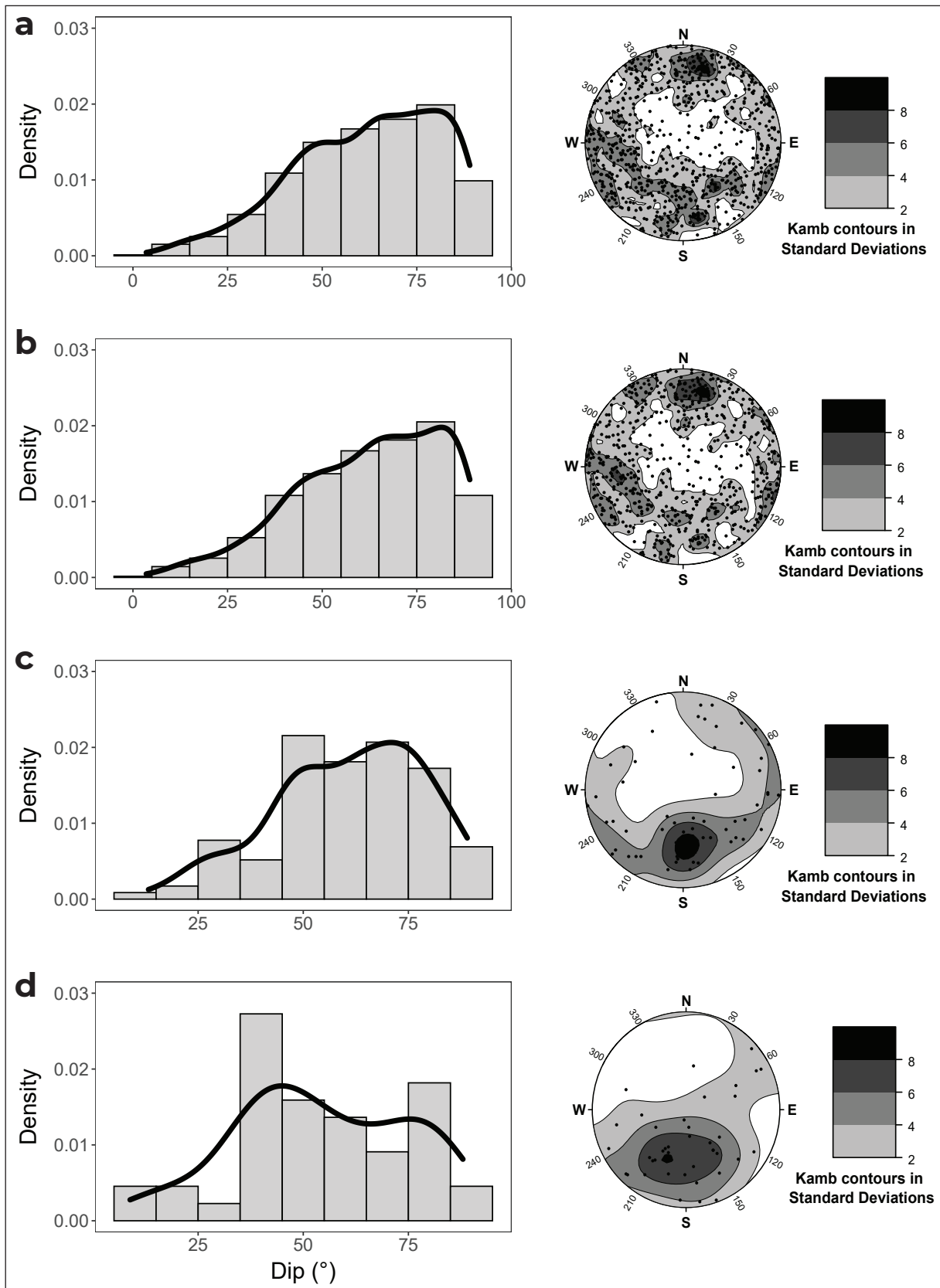
Figure 6. Kamb-contoured projected poles of scanline data by fracture category: **(a)** all fractures, **(b)** open fractures, **(c)** filled fractures, and **(d)** closed fractures.

Table 1. *Average values of the geometric attributes measured during, or calculated based on, the scanline surveys. CV: coefficient of variation; S.D.: standard variation.*

	Linear Intensity (m⁻¹)		Spacing	Length (m)		Aperture (mm)	
	Median	Range	CV	Mean	S.D.	Mean	S.D.
All	13.7	3.8 – 55.6	1.6	0.8	5.9	2.0	3.4
Open	11.3	2.1 – 42.6	1.6	0.9	6.7	2.2	3.7
Filled	3.3	1.1 – 19.4	1.5	0.4	0.4	1.5	1.3
Closed	1.9	0.3 – 9.7	1.6	0.1	0.1	0	0

Table 2. *Qualitative classification of fracture apertures based on ISRM (1978) fracture aperture classification.*

Aperture (mm)	Classification	Measured Fracture Apertures (%)
0	Closed	8
< 0.1	Very tight	1
0.1 – 0.25	Tight	1
0.25 – 0.50	Partly open	9
0.50 – 2.50	Open	20
2.50 – 10	Moderately wide	60
> 10	Wide	1
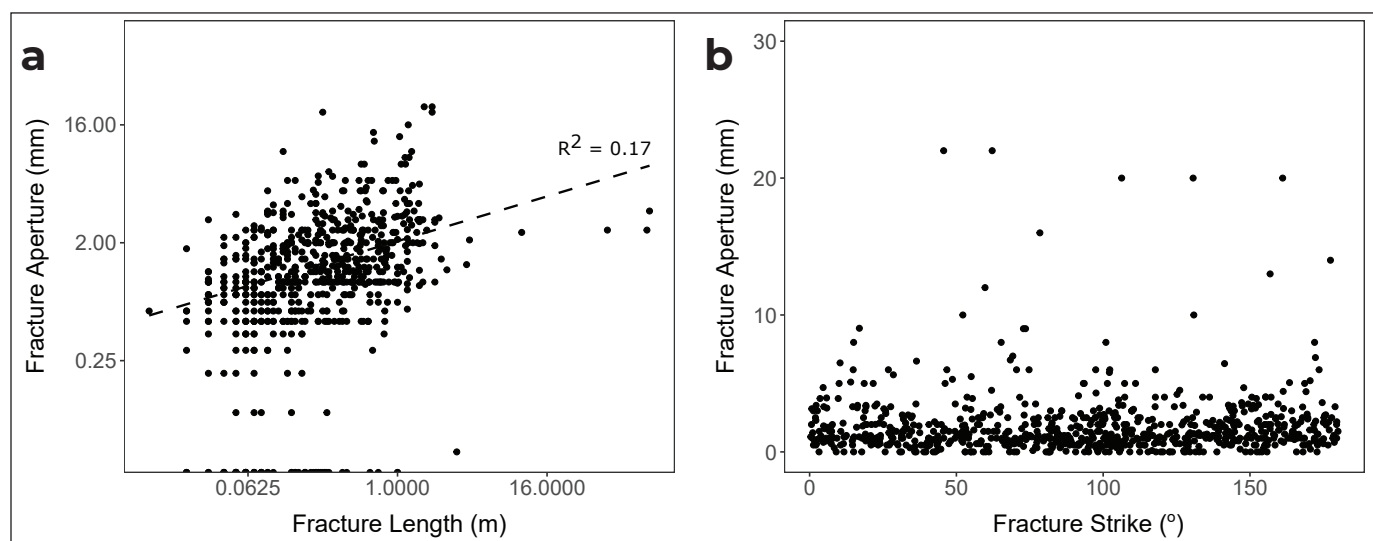
Figure 7. *Fracture aperture scale and strike dependence relative to **(a)** fracture length (fitted with a power-law distribution), and **(b)** fracture strike.*

Geometric fracture attribute variation by lithology and distance from Denali fault

Lithology

The influence of lithology (Appendix B) and distance from the Denali fault on geometric fracture attributes is illustrated in Figure 8. Each geometric attribute was tested to confirm if they met the required assumptions for an analysis of covariance (ANCOVA; Fig. 9; Table 3). The ANCOVA test was only applied on the three dominant rock types and within the first 4 km where sufficient data allowed statistical relevance.

The correlation of all geometric attributes by distance is poor, with certain exceptions. There are moderate positive and negative correlations of linear fracture intensity with increasing distance from the Denali fault for the Station Creek and Hasen Creek formations, respectively. The Nikolai formation has a weak to moderate correlation and also shows a decrease in linear fracture intensity with increasing distance from the Denali fault. Spacing is intrinsically related to the linear fracture intensity but the coefficient of variation (CV) describes the heterogeneity of fracture distribution (Glaas et *al.*, 2021). The heterogeneity of fracture spacing increases in both the Hasen Creek and Nikolai formations but decreases in the Station Creek Formation with respect to the distance from the fault. There is no correlation between fracture mineralization and distance from the fault for any units. The Hasen Creek Formation has a weak to moderate positive correlation with fracture length, and a weak to moderate negative correlation with fracture aperture. The Nikolai formation shows a weak positive correlation such that aperture may increase farther from the fault.

Linearity is an important assumption for an ANCOVA test. The other assumptions are presented in Table 3. Testing for homogeneity of regression slopes confirms a significant interaction between distance and unit for linear fracture intensity. Therefore, the influence of units cannot be evaluated independently of the distance. There is no significant interaction between distance and unit with respect to the coefficient of variation of fracture spacing, mineralization, fracture length, or fracture aperture. However, neither mineralization nor fracture length residuals are normally distributed therefore an ANCOVA test cannot be applied. A complete ANCOVA test may only be applied to the fracture spacing (CV) and fracture aperture as the data distribution respects all of the assumptions.

After controlling for distance, there was not a significant difference in the coefficient of variation of fracture spacing between the major units ($F_{(2,20)} = 1.90$, $p = 0.18$). There was a significant difference in the fracture aperture of the Station Creek, Nikolai and Hasen Creek formations ($F_{(2,20)} = 5.04$, $p < 0.10$). Based on a post-hoc test, there is no significant difference in fracture aperture between the Nikolai formation and the Skolai Group (Station Creek and Hasen Creek formations), but there is a significant difference within the Skolai Group between Station Creek and Hasen Creek formations at a 90% confidence interval.
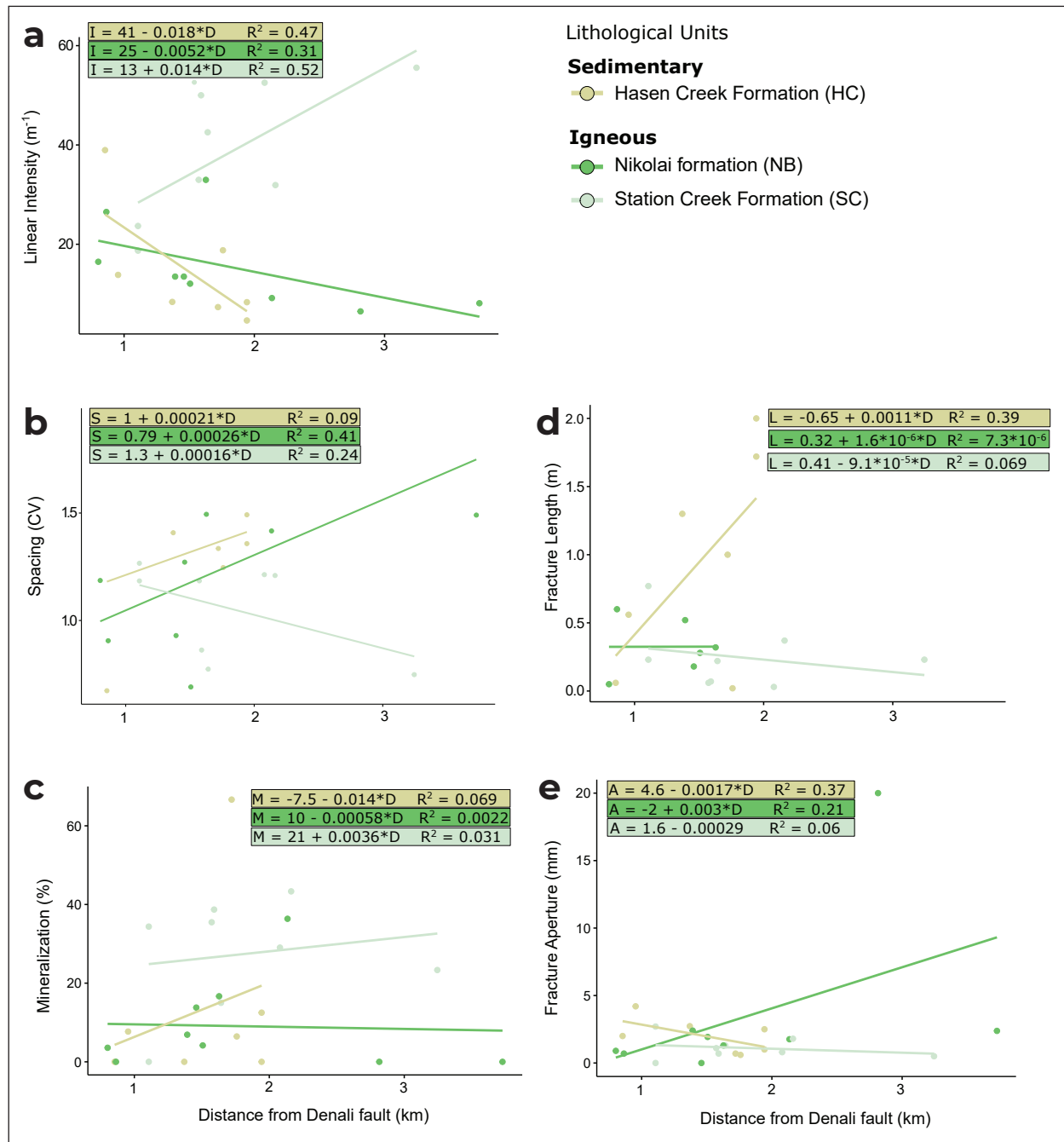
The mean of geometric fracture attributes, without considering distance are presented in Appendix B. The following analysis describes the influence of lithology on geometric attributes over the complete study area. This analysis was not controlled for distance. However, based on a 90% confidence interval, there is a significant difference in linear fracture intensity between Station Creek Formation and both the Hasen Creek and Nikolai formations. There are no significant differences in coefficients of variance for fracture spacing (CV), fracture length, or fracture aperture between the units (Table 4).

Distance

The influence of distance from the Denali fault is non-linear and summarized by distance interval (Table 4). Eight distance categories were created to represent available data. Based on Figure 8 and Table 5, there is a general decrease in linear fracture intensity with distance from the fault, however the variability is significant and must be considered. This variability occurs within and between rock types. The distance from the Denali fault has a negligible influence on fracture spacing and fracture length. Mean fracture aperture is constant with little variability within the first 4 km from the fault. The fracture aperture farther than 4 km from the fault is greater with greater standard deviation.
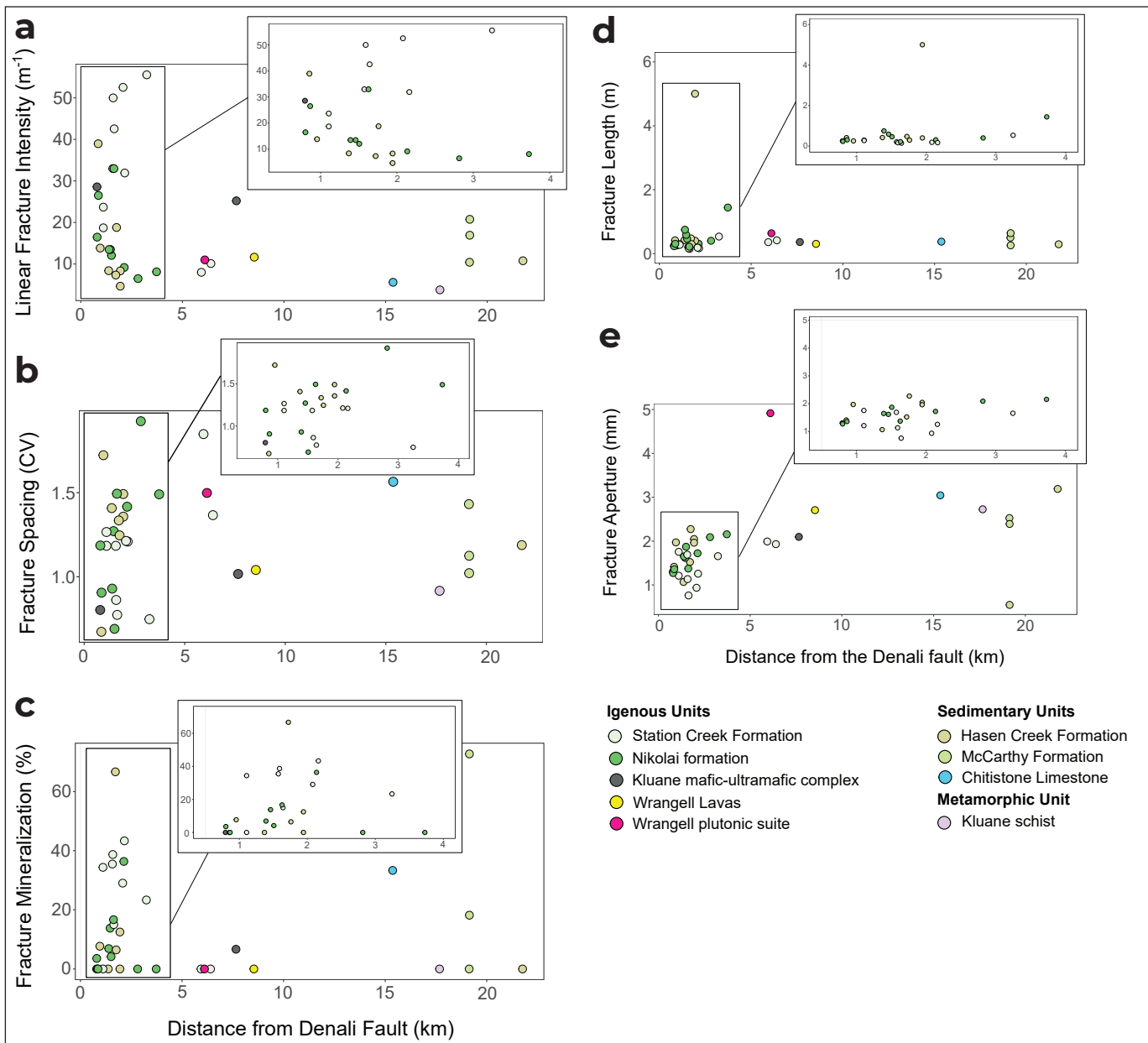
Figure 8. Representation of the influence of lithology and distance from the Denali fault on geometric fracture attributes: (a) Linear fracture intensity, (b) fracture spacing, (c) fracture mineralization, (d) fracture length, and (e) fracture aperture. Large plots show all of the data collected, whereas the inset plots focus on the first 4 km from the Denali fault where the concentration of data points is greatest. This reduces the number of rock types represented, but the three dominant rock types in the region Nikolai formation, Station Creek Formation and Hasen Creek Formation, are all represented within 4 km of the fault. landscape

Figure 9. *Test for linearity of each geometric fracture attribute per lithology within the first 4 km of the Denali fault. The geometric fracture attributes evaluated are:* **(a)** *linear fracture intensity,* **(b)** *fracture spacing (CV),* **(c)** *mineralization,* **(d)** *fracture length, and e) fracture aperture.*

Table 3. *Assumptions required to perform an ANCOVA test. All assumptions must be true with no outliers to be able to control for the covariate (distance). A statement is considered to be TRUE if it falls within a 90% confidence interval.*

Assumptions	Linear Intensity (m⁻¹)	Spacing (CV)	Mineralization (%)	Length (m)	Aperture (mm)
Homogeneity of regression slopes	FALSE	TRUE	TRUE	TRUE	TRUE
Normality of residuals	TRUE	TRUE	FALSE	FALSE	TRUE
Homogeneity of variances	TRUE	TRUE	TRUE	TRUE	TRUE
Outliers	No outliers	No outliers	One outlier M = 66.7% at 1721 m (HC)	One outlier: L = 5.003 at 1943 m (HC)	No outliers

Table 4. *Pairwise t-test to compare geometric fracture attributes for units for which there were two or more scanlines over the complete study area: (a) linear fracture intensity, (b) coefficient of variation of fracture spacing, (c) fracture length, and (d) fracture aperture. Units are abbreviated to: HC (Hasen Creek Formation), KMUM (Kluane mafic-ultramafic complex), McC (McCarthy Formation), NB (Nikolai formation), SC (Station Creek Formation).*

(a) Linear fracture intensity

(t-value)	HC	KMUM	McC	NB
KMUM	1.0	---	---	---
McC	1.0	1.0	---	---
NB	1.0	1.0	1.0	---
SC	0.04	1.0	0.55	0.06

(b) Fracture spacing (CV)

(t-value)	HC	KMUM	McC	NB
KMUM	1.0	---	---	---
McC	1.0	1.0	---	---
NB	1.0	1.0	1.0	---
SC	1.0	1.0	1.0	1.0

(c) Fracture length

(t-value)	HC	KMUM	McC	NB
KMUM	1.0	---	---	---
McC	0.96	1.0	---	---
NB	0.37	1.0	1.0	---
SC	0.12	1.0	1.0	1.0

(d) Fracture aperture

(t-value)	HC	KMUM	McC	NB
KMUM	1.0	---	---	---
McC	1.0	1.0	---	---
NB	1.0	1.0	1.0	---
SC	0.66	1.0	1.0	1.0

Table 5. *Linear fracture intensity summarized by distance. Distance is grouped into two ranges at 1 km intervals close to the fault (0–2 km), 3 ranges of 3 km intervals mid-distance from the fault (2–11 km), and one range greater than 11 km for scanlines recorded far from the fault. The count represents the number of scanlines which fall into the distance range. S.D.: standard variation*

Distance group (km)	Linear Fracture Intensity (m^{-1})		Coefficient of variance fracture spacing		Fracture Length (m)		Fracture Aperture (mm)		Count
	Mean	S.D.	Mean	S.D.	Mean	S.D.	Mean	S.D.	
[0, 1[	24.9	10.1	1.1	0.4	0.3	0.3	1.5	0.3	5
[1, 2[	20.5	14.1	1.2	0.3	0.6	0.6	1.6	0.4	14
[2, 4[	27.3	22.7	1.3	0.4	0.2	0.2	1.6	0.5	6
[4, 7[	9.7	1.5	1.6	0.2	0.4		2.9	1.7	3
[7, 10[	18.4	9.6	1.0	0.02	0.5	0.6	2.4	0.4	2
[10, 30[	11.4	6.5	1.2	0.2	0.4	0.3	2.4	1.0	6

Influence of subsidiary faults on fracture density and aperture

Linear fracture intensity and fracture aperture have been shown to have the greatest control on permeability. The Denali fault is the major regional fault, but there are also numerous smaller faults. These subsidiary faults likely contribute to the variability in geometric fracture attributes (Fig. 10). The linear fracture intensity is smallest in outcrops along Burwash Creek where the distance between the Denali fault and the first subsidiary fault is the greatest; these are followed by outcrops at Copper Joe Creek. The variation in fracture aperture does not seem to be related to the subsidiary faults.

Discussion

Fracture orientation

Fault networks typically consist of two to three fracture families, whereas joint networks can consist of one to an indistinguishable number of fracture families (Berkowitz et a*l.*, 2000). On outcrops in the Duke River area some minor faults were noted, but fracture networks consisted mainly of joints and veins.

The dip of the Denali fault has not been defined but this strike-slip fault is assumed to be near-vertical. The fractures in the Duke River area are steeply dipping which is consistent with the geological environment in which they were formed. Steep fractures in steeply dipping fault zones can increase vertical permeability which is favourable to convective heat transport that can potentially increase near-surface temperature gradients (Timar-Geng et a*l.*, 2009).

Average fracture attributes

The geometric fracture attributes, density, spacing (CV), length and aperture of open fractures control present-day permeability. The mean linear fracture intensity of open fracture in the Duke River area is significantly higher (11.3 frac m^{-1}) compared to other naturally fractured geothermal reservoirs. For example, the crystalline reservoir rocks in the northern Upper Rhine Graben (2.17 frac m^{-1}; Bossennec et a*l.*, 2022), Saint Pierre Bois Quarry (0.79 frac m^{-1}; Dezayes et a*l.*, 2021), or in the Central Upper Rhine Graben (~0.76 frac m^{-1}; Glaas et a*l.*, 2021) all have lower linear fracture intensity. The fracture density distribution is described based on fracture spacing (Gillespie et a*l.*, 1999; Odling et a*l.*, 1999). In the Duke River area, the fracture spacing is heterogeneous and poorly clustered.

Figure 10. *Linear fracture intensity per scanline collected on foot at outcrops located along creeks. These indicate the proximity of each outcrop to faults in addition to the Denali fault. These include the Bock's Creek and unnamed faults.*

The distribution of fracture lengths is central to developing stochastic discrete fracture networks and evaluating secondary permeability (e.g., Bour and Davey, 1997; Bonnet et a*l*., 2001; Darcel et a*l*., 2003). The distribution of fracture lengths can inform whether connectivity is controlled by small fractures, large fractures, or equally by both small and large fractures (Bour and Davey, 1997).

Fracture length is related to fracture aperture wherein longer fractures typically have greater aperture. The association between fracture length and aperture is integrated into discrete fracture models (Bossennec et a*l*., 2022). However, the aperture of shear-dependent fractures has also been shown to depend on the maximum horizontal stress direction such that fractures oriented parallel to the maximum stress direction exhibit apertures two to three times greater than fractures oriented perpendicular to the maximum stress direction (Reinecker et a*l*., 2021). As a result, fractures oriented parallel to the maximum stress direction act as preferential flow pathways (Reinecker et a*l*., 2021).

Regional scale focal mechanism data indicate a NE-SW dominant compressive stress direction in southwestern Yukon (Ristau et a*l*., 2007). Based on the focal mechanism data available and a localized stress inversion around the eastern Denali fault near Duke River, the maximum compressive stress direction (N50°E) is nearly perpendicular to the eastern Denali fault (T. Finley, personal communication). This orientation is consistent with the results of Choi et a*l*. (2021) in northwestern British Columbia ~200 km to the southeast. Therefore, open fractures oriented around N50°E would be expected to have a greater fracture aperture than open fracture oriented around N140°E. Based on the scanline data, there is no correlation between fracture aperture and orientation, but surface weathering likely camouflage the true fracture aperture.

The effect of weathering on surface outcrops causes fracture aperture measured on outcrops to consistently overestimate subsurface aperture, even if corrected for pressure (Peacock et a*l*., 2022). Comparably, drilling mechanically erodes the surface of fracture rims on the well wall but fracture apertures are preserved in the drill core (Glaas et a*l*., 2021). Therefore, further aperture analysis on drill core is required to confirm fracture aperture and detect any preferential strike for wider aperture fractures.

Potential for permeability based on described fracture data

The geometric fracture attributes described will be fitted into a small-scale discrete fracture model to determine the permeability (e.g., Bossennec et a*l*., 2022). However, modelling large-scale fracture networks requires a lot of computational power. In a regional groundwater flow model, the permeability may be described by an equivalent porous media. This data set may be well suited to be represented as an equivalent porous media due to the high fracture density and homogeneous fracture distribution in all orientations (Zareidarmiyan et a*l*., 2021).

Before developing a discrete fracture model, a first-order estimation of permeability can be deduced based on fractured areas with similar conditions. For example, pemeability was determined to range between 1×10^{-17} and 1.1×10^{-16} m^2 in the Upper Rhine Graben where significantly lower fracture density was reported (Bossennec et a*l*., 2022). The permeability of the Upper Rhine Graben is slightly lower than the typical permeability of moderately fractured low-porosity rocks (10^{-15} m^2; Forster and Smith, 1989). Therefore, we can expect the permeability of the Duke River area to be at least on the order of 10^{-15} m^2. The steeply dipping fractures can create an anisotropy such that the near-vertical permeability exceeds the horizontal permeability (Lazear, 2009). A combination of steep fractures and high permeability is known to facilitate forced convection in mountainous regions (Forster and Smith, 1989; Timar-Geng et a*l*., 2009).

Influence of lithology and distance on geometric fracture attributes

Herein, fracture data were analyzed as a whole, by lithology, and by distance from the fault. This was an important distinction as previous research in the Central Upper Rhine Graben has shown that linear fracture intensity varied by lithology (Glaas et a*l.*, 2021). In the Central Upper Rhine Graben, linear fracture intensity was lower in the sedimentary unit (sandstone) than in the igneous unit (granite). This comparison is more complex in the Duke River area as we need to consider the influence of distance from the Denali fault. The only parameter that met the assumptions to be controlled for distance over the first four kilometres from the Denali fault, where data were abundant, was the fracture aperture. The Hasen Creek and Nikolai formations could be grouped as they are significantly different from the Station Creek Formation; however this variation is not significant over the whole study area, when not controlled for the influence of distance from the Denali fault.

There are only significant variations in the linear fracture intensity when considering the whole study area without controlling for distance. However, this is not aligned with Glaas et a*l.* (2021) observations as the significant difference are between two volcanic units (Station Creek and Nikolai formations). Rather than simplifying the regional geology to rock types, our results show that there is only significant difference between the Station Creek Formation and other rock types. Therefore, when considering linear fracture intensity in the conceptual model, rock types can be grouped into Station Creek Formation (Group 1) and a combination of all other major units (Group 2; including the Hasen Creek, Nikolai and McCarthy formations, and the Kluane mafic-ultramafic complex).

Insufficient to no data were collected on three sedimentary units in the cross sections of interest: Hoge Creek succession, Tatamagouche succession and Quaternary deposits. The Hoge succession overlies the Hasen Creek Formation (Fig. 3) and is included in Group 2 to consider linear fracture intensity. The Tatamagouche succession and Quaternary deposits are surficial units. The Tatamagouche succession coverage is sparse and is expected to have little influence on deep groundwater circulation. The permeability of Quaternary deposits is controlled by primary porosity.

There was not a significant difference in the coefficient of variance for fracture spacing and fracture length between rock types. Therefore, only the influence of distance will be considered for these attributes. Fracture aperture increased non-linearly with increasing distance from the Denali fault (Table 5). The fracture apertures will be considered in two groups: within 4 km from the Denali fault and farther than 4 km from the Denali fault.

Influence of subsidiary faults on linear fracture density and aperture

Herein, we assumed that the dominant stress field was related to the Denali fault. However, other faults have been mapped in the Duke River area and there is regional compressional deformation in the St. Elias region that contributes to the continuous exhumation of the St. Elias mountain ranges southwest of the Duke River area. This regional compression likely contributes to the variation in measured fracture networks. The statistical significance of proximity of fractures to subsidiary faults was not evaluated. However, there is a general trend of high linear fracture intensity when subsidiary faults are closer together (e.g., Fig. 10b,f), compared to when faults are farther apart (e.g., Fig. 10a,c).

Conclusions

Overall, linear fracture intensity in the Duke River area is high and open fractures are equally oriented in all directions. The linear fracture intensity, and other geometric fracture attributes (fracture spacing, length and aperture) influence large-scale permeability. Based on the fracture analysis completed in this work, rock types with similar attributes can be grouped into two main hydrostratigraphic units of a conceptual

groundwater flow model. Group 1 only includes the Station Creek Formation, and Group 2 includes all other rock types. The fracture spacing and fracture length attributes are independent of the distance from the Denali fault. There is a weak non-linear correlation between distance from the Denali and both fracture intensity and fracture aperture wherein fracture density is greatest within the first 4 km of the fault, but fracture aperture is greatest farther than 4 km from the Denali fault. This relationship is weak, and fractures may also be associated to other faults and the exhumation of the Saint Elias Mountains, which contributes to the above-average fracture intensity of the area.

These conclusions were drawn based on scanline data distributed over the study area at 0.8 km to 22 km from the Denali fault. This data set lacks fracture measurements within the first 750 m from the Denali fault due to extensive Quaternary sediment coverage and farther than 5 km due to outcrop accessibility constraints. The data gap next to the Denali fault could be filled by analysis of drill core from exploration boreholes. The core would also improve fracture aperture data as current fracture aperture measurements were recorded on weathered outcrops.

Ultimately, the orientation and geometric fracture attributes described herein will be used to develop a discrete fracture network and evaluate large scale permeability. Thereafter, future research will integrate these results into a hydrothermal model to evaluate the deep geothermal potential in the Duke River area.

References

Allmendinger, R.W., 2022. Stereonet 11.4.5. Software, https://www.rickallmendinger.net/stereonet.

Andrews B.J., Roberts J.J., Shipton Z.K., Bigi S., Tartarello M.C. and Johnson G., 2019. How do we see fractures? Quantifying subjective bias in fracture data collection. Solid Earth, vol. 10, p. 487–516, https://doi.org/10.5194/se-10-487-2019.

Bender, A.M. and Haeussler, P.J., 2017. Eastern Denali Fault Surface Trace Map, Eastern Alaska and Yukon, Canada. U.S. Geological Survey, Open-File Report 2017-1049, 10 p., https://doi.org/10.3133/ofr20171049.

Beranek, L.P. and Mortensen, J.K., 2011. The timing and provenance record of the late Permian Klondike Orogeny in northwestern Canada and arc-continent collision along Western North America. Tectonics, vol. 30, https://doi.org/10.1029/2010tc002849.

Berkowitz, B., Bour, O., Davy, P. and Odling, N., 2000. Scaling of fracture connectivity in geological formations. Geophysical Research Letters, vol. 27, p. 2061–2064, https://doi.org/10.1029/1999GL011241.

Blais-Stevens, A., Clague, J.J., Brahney, J., Lipovsky, P., Haeussler, P.J. and Menounos, B., 2020. Evidence for Large Holocene Earthquakes along the Denali Fault in Southwest Yukon, Canada. Environmental & Engineering Geoscience, vol. 26, p. 149–166, https://doi.org/10.2113/EEG-2263.

Bonnet, E., Bour, O., Odling, N.E., Davy, P., Main, I., Cowie, P. and Berkowitz, B., 2001. Scaling of Fracture Systems in Geological Media. Reviews of Geophysics, vol. 39, p. 347–383, https://doi.org/10.1029/1999RG000074.

Bossennec, C., Seib, L., Frey, M., van der Vaart, J. and Sass, I., 2022. Structural Architecture Permeability Patterns of Crystalline Reservoir Rocks in the Northern Upper Rhine Graben: Insights from Surface Analogues of the Odenwald. Energies, vol. 15, https://doi.org/10.3390/en15041310.

Bour, O. and Davey, P., 1997. Connectivity of random fault networks following a power law fault length distribution. Water Resources Research, vol. 33, p. 1567–1583, https://doi.org/10.1029/96WR00433.

Camanni, G., Vinci, F., Tavani, S., Ferrandino, V., Mazzoli, S., Corradetti, A., Parente, M. and Iannace, A., 2021. Fracture density variations within a reservoir-scale normal fault zone: A case study from shallow-water carbonates of southern Italy. Journal of Structural Geology, vol. 151, https://doi.org/10.1016/j.jsg.2021.104432.

Chabani, A., Mehl, C., Cojan, I., Alais, R. and Bruel, D., 2020. Semi-automated component identification of a complex fracture network using a mixture of von Mises distributions: Application to the Ardeche margin (South-East France). Computers & Geoscience, vol. 137, https://doi.org/10.1016/j.cageo.2020.104435.

Chakraborty, S. and Wong, S.W., 2021. BAMBI: an R Package for Fitting Bivariate Angular Mixture Models. Journal of Statistical Software, vol. 99, https://doi.org/10.18637/jss.v099.i11.

Choi, M., Eaton, D.W. and Enkelmann, E., 2021. Is the Eastern Denali fault still active? Geology, vol. 49, 5 p., https://doi.org/10.1130/G48461.1.

Colpron, M., Crowley, J.L., Gehrels, G.E., Long, D.G.F., Murphy, D.C., Beranek, L.P. and Bickerton, L., 2015. Birth of the northern Cordilleran orogen, as recorded by detrital zircons in Jurassic synorogenic strata and regional exhumation in Yukon. Lithosphere, vol. 7, p. 541–562, https://doi.org/10.1130/L451.1.

Colpron, M., Israel, S. and Friend, M., 2016. Yukon plutonic suites. Yukon Geological Survey, Open File 2016-37, scale 1:750 000.

Colpron, M., Nelson, J. L. and Murphy, D. C., 2007. Northern Cordillera terranes and their interactions through time. GSA Today, vol. 17, p. 4–10, https://doi.org/10.1130/GSAT01704-5A.1.

Colpron, M., Sack, P.J., Crowley, J.L., Beranek, L.P. and Allan, M.M., 2022. Late Triassic to Jurassic magmatic and tectonic evolution of the Intermontane terranes in Yukon, northern Canadian Cordillera: Transition from arc to syn-collisional magmatism and post-collisional lithospheric delamination. Tectonics, vol. 41, https://doi.org/10.1029/2021TC007060.

Darcel, C., Bour, O. and Davy, P., 2003. Stereological analysis of fractal fracture networks. Journal of Geophysical Research: Solid Earth, vol. 108, https://doi.org/10.1029/2002JB002091.

Dezayes, C., Lerouge, C., Innocent, C. and Lach, P., 2021. Structural control on fluid circulation in a graben system: Constraints from the Saint Pierre Bois quarry (Vosges, France). Journal of Structural Geology, vol. 146, https://doi.org/10.1016/j.jsg.2021.104323.

Elliott, J.L., Larsen, C. F., Freymueller, J.T. and Motyka, R. J., 2010. Tectonic block motion and glacial isostatic adjustment in southeast Alaska and adjacent Canada constrained by GPS measurements. Journal of Geophysical Research: Solid Earth, vol. 115, https://doi.org/10.1029/2009JB007139.

Faulds, J.E. and Hinz, N.H., 2015. Favorable Tectonic and Structural Settings of Geothermal Systems in the Great Basin Region, Western USA: Proxies for Discovering Blind Geothermal Systems. Proceedings World Geothermal Congress 2015, Melbourne, Australia, April 2015.

Finley, T., Salomon, G., Stephen, R., Nissen, E., Cassidy, J. and Menounos, B., 2022. Preliminary results and structural interpretations from drone lidar surveys over the Eastern Denali fault, Yukon. Yukon Exploration and Geology 2021, K.E. MacFarlane (ed.), Yukon Geological Survey, p. 83–105.

Formenti, S., Peace, A., Eyles, C., Lee, R. and Waldron, J., 2022. Fractures in the Niagara Escarpment in Ontario, Canada: distribution, connectivity, and geohazard implications. Geological Magazine, https://doi.org/10.1017/S0016756822000462.

Forster, C. and Smith, L., 1989. The Influence of Groundwater Flow on Thermal Regime in Mountainous Terrain: A Model Study. Journal of Geophysical Research: Solid Earth, vol. 94, p. 9439–9451, https://doi.org/10.1029/JB094iB07p09439.

Fossen, H., 2010. Structural geology: First Edition. Cambridge University press.

George, S.W.M., Nelson, J.L., Alberts, D., Greig, C.J. and Gehrels, G.E., 2021. Triassic-Jurassic Accretionary History and Tectonic Origin of Stikinia from U-Pb Geochronology and Lu-Hf isotope Analysis, British Columbia. Tectonics, vol. 40, https://doi.org/10.1029/2020tc006505.

Gillespie, P.A., Johnston J.D., Loriga, M.A., McCaffrey, K.L.W., Walsh, L.L. and Watterson, L., 1999. Influence of layering on vein systematics in line samples. *In*: Fractures, Fluid Flow and Mineralization, K. McCaffrey, L. Lonergan and J.J. Wilkinson (eds.), Geological Society, London, Special Publication No. 155, p. 35–56, https://doi.org/10.1144/GSL.SP.1999.155.01.05.

Glaas, C., Vidal, J. and Genter, A., 2021. Structural characterization of naturally fractured geothermal reservoirs in the central Upper Rhine Graben. Journal of Structural Geology, vol. 148, https://doi.org/10.1016/j.jsg.2021.104370.

Haeussler, P.J., Matmon, A., Schwartz, D.P. and Seitz, G.G., 2017. Neotectonics of interior Alaska and the late Quaternary slip rate along the Denali fault system. Geosphere, vol. 13, p. 1445–1463, https://doi.org/10.1130/GES01447.1.

Haneberg, W.C., 2004. Special Plots for Geoscience Data. *In:* Computational Geosciences with Mathematica. Springer, Berlin, Heidelberg, p. 25–55, https://doi.org/10.1007/978-3-642-1854-0_2.

Israel, S., Tizzard, A. and Major, J., 2006. Bedrock Geology of the Duke River area, parts of NTS 115G/2, 3, 4, 6 and 7, southwestern Yukon. *In:* Yukon Exploration and Geology 2005, D.S. Emond, G.D. Bradshaw, L.L. Lewis and L.H. Weston (eds.), Yukon Geological Survey, p. 139–154.

Lazear, G.D., 2008. Fractures, convection and underpressure: hydrogeology on the southern margin of the Piceance basin, west-central Colorado, USA. Hydrogeology Journal, vol. 17, p. 641–664, https://doi.org/10.1007/s10040-008-0381-3.

Leonard, L.J., Mazzotti, S. and Hyndman, R.D., 2008. Deformation rates estimated from earthquakes in the northern Cordillera of Canada and eastern Alaska. Journal of Geophysical Research: Solid Earth, vol. 113, https://doi.org/10.1029/2007JB005456.

Lowey, G.W., 1998. A new estimate of the amount of displacement on the Denali fault system based on the occurrence of carbonate megaboulders in the Dezadeash Formation (Jura-Cretaceous), Yukon, and the Nutzotin Mountains sequence (Jura-Cretaceous), Alaska. Bulletin of Canadian Petroleum Geology, vol. 46, p. 379–386, https://doi.org/10.35767/gscpgbull.46.3.379.

Marechal, A., Ritz, J.-F., Ferry, M., Mazzotti, S., Blard, P.-H., Braucher, R. and Saint-Carlier, D., 2018. Active tectonics around the Yakutat indentor: New geomorphological constraints on the eastern Denali, Totschunda and Duke River Faults. Earth and Planetary Science Letters, vol. 482, p. 71–80, https://doi.org/10.1016/j.epsl.2017.10.051.

McDermott, R.G., Ault, A.K., Caine, J.S. and Thomson, S. N., 2019. Thermotectonic History of the Kluane Ranges and Evolution of the Eastern Denali Fault Zone in Southwestern Yukon, Canada. Tectonics, vol. 38, p. 2983–3010, https://doi.org/10.1029/2019TC005545.

Mezger, J.E., Creaser, R.A., Erdmer, P. and Johnston, S.T., 2001a. A Cretaceous back-arc basin in the Coast belt of the northern Canadian Cordillera: evidence from geochemical and neodymium isotope characteristics of the Kluane metamorphic assemblage, southwest Yukon. Canadian Journal of Earth Sciences, vol. 38, p. 91–103, https://doi.org/10.1139/e00-076.

Mezger, J.E., Chacko, T. and Erdmer, P., 2001b. Metamorphism at a late Mesozoic accretionary margin: a study from the Coast belt of the North American Cordillera. Journal of metamorphic Geology, vol. 19, p. 121–137, https://doi.org/10.1046/j.0263-4929.2000.00300.x.

Morgan, P., Harder, V., Swanberg, C.A. and Daggett, P.H., 1981. Groundwater convection model for Rio Grande rift geothermal resources. *In:* Geothermal Direct Heat Program: Glenwood Springs Technical Conference Proceedings, Volume 1. Papers Presented State Coupled Geothermal Resource Assessment Program, p. 228–231, https://www.geothermal-library.org/index.php?mode=pubs&action=view&record=1013845.

Nelson, J. and Colpron, A., 2007. Tectonics and Metallogeny of the British Columbia, Yukon, and Alaskan Cordillera, 1.8 Ga to the Present. *In:* Mineral Deposits of Canada: A Synthesis of Major Deposit-Types, District Metallogeny, the Evolution of Geological Provinces, and Exploration Methods, W.D. Goodfellow (ed.), Geological Association of Canada, Special Publication No. 5, p. 755–791.

Odling, N.E., Gillespie, P., Bourgine, B., Castaing, C., Chiles, J.P., Christensen, N.P., Fillion, E., Genter, A., Olsen, C., Thrane, L., Trice, R., Aarseth, E., Walsh, J.J. and Watterson, J., 1999. Variations in fracture system geometry and their implications for fluid flow in fractured hydrocarbon reservoirs. Petroleum Geoscience, vol. 5, p. 373–384, https://doi.org/10.1144/petgeo.5.4.373.

Peacock, D.C.P., Sanderson, D.J. and Leiss, B., 2022. Use of Analogue Exposures of Fractured Rock for Enhanced Geothermal Systems. Geosciences, vol. 12, https://doi.org/10.3390/geosciences12090318.

Reinecker, J., Gutmanis, J., Foxford, A., Cotton, L., Dalby, C. and Law, R., 2021. Geothermal exploration and reservoir modelling of the United Downs deep geothermal project, Cornwall (UK). Geothermics, vol. 97, https://doi.org/10.1016/j.geothermics.2021.102226.

Ristau, J., Rogers, G.C. and Cassidy, J.F., 2007. Stress in western Canada from regional moment tensor analysis. Canadian Journal of Earth Sciences, vol. 44, p. 127–148, https://doi.org/10.1139/e06-057.

Saar, M., 2010. Review: Geothermal heat as a tracer of large-scale groundwater flow and means to determine permeability fields. Hydrogeology Journal, vol. 19, p. 31–52, https://doi.org/10.1007/s10040-010-0657-2.

Sanderson, D.J. and Peacock, D.C.P., 2019. Line sampling of fracture swarms and corridors. Journal of Structural Geology, vol. 122, p. 27–37, https://doi.org/10.1016/j.jsg.2019.02.006.

Singhal, B.B.S. and Gupta, R.P., 2010. Applied Hydrogeology of Fractured Rocks: Second Edition. Springer, https://doi.org/10.1007/978-90-481-8799-7.

Stanley, B., 2012. Structural geology and geochronology of the Kluane schist, southwestern Yukon Territory. Unpublished MSc thesis, University of Waterloo, Ontario, Canada, 113 p.

Štulc, P., 1998. Combined effect of topography and hydrogeology on subsurface temperature — implications for aquifer permeability and heat flow. A study from the Bohemian Cretaceous basin. Tectonophysics, vol. 284, p. 161–174, https://doi.org/10.1016/S0040-1951(97)00171-6.

Tang, H.M., Huang, L., Bobet, A., EzEldin, M.A.M., Wang, L.Q., Wu, Y.P. and Hu, X.L., 2016. Identification and mitigation of error in the Terzaghi Bias Correction for inhomogeneous material discontinuities. Strength of Materials, vol. 48, p. 825–833, https://doi.org/10.1007/s11223-017-9829-9.

Timar-Geng, Z., Henk, A. and Wetzel, A., 2009. Convective heat transfer in a steeply dipping fault zone and its impact on the interpretation of fission-track data – a modelling study. In: Thermochronological Methods: From Palaeotemperature Constraints to Landscape Evolution Models, Geological Society of London, Special Publications 324, p. 87–98. https://doi.org/10.1144/SP324.7.

Townend, J. Sutherland, R., Toy, V.G., Doan, M.L., et al., 2017. Petrophysical, geochemical, and hydrological, evidence for extensive fracture-mediated fluid and heat transport in the Alpine Fault's hanging-wall damage zone. Geochemistry, Geophysics, Geosystems, vol. 18, p. 4709–4732, https://doi.org/10.1002/2017GC007202.

Tschirhart, V., Colpron, M., Craven, J., Ghalati, F.H., Enkin, R.J. and Grasby, S.E. 2022. Geothermal Exploration in the Burwash Landing Region, Canada, Using Three-Dimensional Inversion of Passive Electromagnetic Data. Remote Sensing, vol. 14, https://doi.org/10.3390/rs14235963.

Vaughn, A., Collins, N., Krus, M. and Rourke, P., 2014. Recent Development of an Earth Science App – FieldMove Clino. EGU General Assembly 2014, Vienna, Austria, April 27–May 2, 2014.

Waldien, T.S., Roeske, S.M. and Benowitz, J.A., 2021. Tectonic underplating and dismemberment of the Maclaren-Kluane schist records Late Cretaceous terrane accretion polarity and ~480 km of post-52 Ma dextral displacement on the Denali fault. Tectonics, vol. 40, https://doi.org/10.1029/2020TC006677.

Watkins, H., Bond, C.E., Healy, D. and Butler, W.H., 2015. Appraisal of fracture sampling methods and a new workflow to characterise heterogeneous fracture networks at outcrop. Journal of Structural Geology, vol. 72, p. 67–82, https://doi.org./10.1016/j.jsg.2015.02.001.

Witter, J.B., 2020. Early-stage exploration for geothermal energy resources along the Denali fault near Duke River, Yukon. Yukon Geological Survey, Open File 2020-3, 62 p.

Yukon Geological Survey, 2020. A digital atlas of terranes for the northern Cordillera. Yukon Geological Survey, https://data.geology.gov.yk.ca/Compilation/2, [accessed November 20, 2022].

Yukon Geological Survey, 2022. Yukon Digital Bedrock Geology. Yukon Geological Survey, http://data.geology.gov.yk.ca/Compilation/3, [accessed October 22, 2022].

Zareidarmiyan, A. Parisio, F., Maknenko, R.Y., Salarirad, H. and Vilarrasa, V., 2021. How equivalent are equivalent porous media? Geophysical Research Letters, vol. 48, https://doi.org/10.1029/2020GL089163.

Zeeb, C., Gomez-Rivas, E., Bons, P.D. and Blum, P., 2013. Evaluation of sampling methods for fracture network characterization using outcrops. American Association of Petroleum Geologists Bulletin, vol. 97, p. 1545–1566, https://doi.org/10.1306/02131312042.

Appendix A

Nomenclature

s – number of scanlines

f – number of fracture measurements

S – spacing

a – fracture strike

a' – scanline strike

P – fracture position

L – scanline length

I – linear fracture intensity

N – number of fractures

H – number of fracture families

CV – coefficient of variation

MvM – Mixture von Mises

vM – von Mises

θ – strike (radians)

κ - concentration parameter

f – function

ω – weight

$NLlik$ – Negative Log-likelihood

Subscripts

i – initial/first measurement

f – final/last measurement

Appendix A continued.

The approach used to determine fracture families using a Mixture von Mises distribution (*MvM*) is based on Chabani et al. (2020). A Mixture of von Mises (*MvM*) distribution is the weighted sum of several von Mises (*vM*) distributions, where a von Mises distribution is described by:

$$f(\theta | \mu, \kappa) = \frac{1}{2\pi I_0(\kappa)} e^{\kappa \cos(\theta - \mu)} \tag{A1}$$

where θ is the simplified strike in radians ($0 \leq \theta \leq \pi$; Eq. 2), μ is the circular mean ($0 \leq \mu \leq \pi$) and κ is the concentration parameter ($\kappa \geq 0$). The parameter $1/\kappa$ is analogous to the standard deviation (σ^2) in a normal distribution.

Here, all fracture strikes have been simplified to range between 0° and 180°, therefore when $a_i > 180°$:

$$a = a_i - 180 \tag{A2}$$

where a_i is the initial azimuth and a is the simplified azimuth. All strikes must be converted to radians such that:

$$\theta = \frac{a 2\pi}{180} \tag{A3}$$

Within the von Mises distribution, I_0 (κ) is the modified Bessel function (Mardia and Jupp, 2000), given by:

$$I_0(\kappa) = \frac{1}{2\pi} \int_0^{2\pi} e^{\kappa \cos\theta} d\theta \tag{A4}$$

In multimodal data sets, the Mixture of Von Mises distribution considers H components such that each component is described by:

$$f_h(\theta) = \frac{1}{2\pi I_0(\kappa_h)} e^{\kappa_h \cos(\theta - \mu_h)} \tag{A5}$$

As the weighted sum of serval von Mises (*vM*) distributions, the Mixture of Von Mises distribution (*MvM*) is given by:

$$MvM_H(\theta) = \sum_{h=1}^{H} \omega_h f_h(\theta) \tag{A6}$$

where H is the number of components and ω_h is the weight of the h_{th} component.

The negative log-likelihood (NLlik) for each *MvM* with different number of components in each fracture category is determined by:

$$NLlik(\theta) = -\sum_{i=1}^{n} \log\left[\sum_{h=1}^{H} \omega_h f_h(\theta_i)\right] \tag{A7}$$

Appendix B

Table B1. *Average values of the geometric attributes measured during, or calculated based on, the scanline surveys by lithology. CV: coefficient of variation.*

Lithology	Linear Intensity (m^{-1})		Spacing (CV)		Length (m)		Aperture (mm)	
(Open)	Median	S.D.	Mean	S.D.	Mean	S.D.	Mean	S.D.
Granodiorite Pluton	11.0	---	1.5	---	0.6	0.5	4.9	5.8
Kluane mafic-ultramafic	26.9	2.4	0.9	0.2	0.3	0.3	1.7	1.3
Nikolai formation	13.5	8.8	1.3	0.4	0.4	0.6	2.2	5.2
Station Creek Formation	32.4	17.4	1.2	0.3	0.2	0.2	1.5	1.9
Wrangell Lavas	11.6	---	1.0	---	0.3	0.2	2.7	3.0
Chitistone Limestone	5.6	---	1.6	---	0.4	0.3	3.0	1.9
Hasen Creek Formation	9.6	11.0	1.3	0.3	0.6	0.6	1.8	2.1
McCarthy Formation	16.9	5.2	1.2	0.2	0.5	0.4	2.0	1.5
Kluane schist	3.8	---	0.9	---	0.7	0.5	2.7	0.5

Table B2. *Average values of the geometric attributes measured during, or calculated based on, the scanline surveys by rock type: igneous and sedimentary. There are insufficient data to summarize metamorphic units. CV: coefficient of variation.*

Lithology	Linear Intensity (m^{-1})		Spacing (CV)		Length (m)		Aperture (mm)	
(Open)	Median	S.D.	Mean	S.D.	Mean	S.D.	Mean	S.D.
Igneous	18.7	15.2	1.2	0.3	0.4	0.2	2.6	1.4
Sedimentary	10.6	9.5	1.3	0.3	0.5	0.1	2.3	0.6